Received: 28 October 2020 | Revised: 26 March 2021 | Accepted: 3 April 2021

DOI: 10.1111/ffe.13474

ORIGINAL ARTICLE

FFEMS Fatigue & Fracture of Engineering Materials & Structures WILEY

Numerical investigation of the effect of holes on dynamic fracturing in multi-flawed granite

Zhongwen Yue[1] | **Jun Zhou**[1] | **Chun Feng**[2] | **Akang Li**[1] | **Peng Qiu**[1] | **Mingwei Gang**[1]

[1]School of Mechanics & Civil Engineering, China University of Mining and Technology (Beijing), Beijing, China

[2]Key Laboratory for Mechanics in Fluid Solid Coupling Systems, Institute of Mechanics, Chinese Academy of Sciences, Beijing, China

Correspondence
Jun Zhou, School of Mechanics & Civil Engineering, China University of Mining and Technology (Beijing), Beijing 100083, China.
Email: jzhou91@163.com

Funding information
National Natural Science Foundation of China, Grant/Award Number: 51974318

Abstract

A numerical study is conducted using the improved continuum-based discrete element method (CDEM) to investigate the effect of holes on the dynamic fracturing of multi-flawed rocks. The specimen geometries contain a perpendicular crack-like flaw, a hole-like flaw, and an inclined crack-like flaw. A fracture model is implemented into the improved CDEM that combines the nonlinear pressure-dependent shear strength and tensile strength of rocks. The digital image correlation method combined with ultra-high-speed photography is applied in a split Hopkinson pressure bar system to verify the accuracy of the proposed model. The experimental results show that the improved CDEM accurately reproduces dynamic crack behavior in rocks. The simulation results show that hole-like flaws significantly affect crack behavior compared with the two investigated crack-like flaws. However, this effect gradually weakens with increasing loading stresses. This study provides important insight into the dynamic fracturing of multi-flawed rocks.

KEYWORDS

continuum-based discrete element method, crack, flawed rock, split Hopkinson pressure bar system

1 | INTRODUCTION

Natural rocks usually contain defects (e.g., fissures, voids, and weak planes) that form during rock genesis and tectonic evolution. Flawed rocks play a significant role in geological engineering. Studies of intact rocks ignore the effect of such defects, which introduces large uncertainties regarding the crack behavior of fractured rock masses. A thorough investigation of the crack behavior in flawed rocks is therefore of significant importance for understanding the fracture mechanism of rock masses.

Numerous experimental studies have been performed to determine the underlying mechanism of crack behavior in flawed rocks,[1–13] and the effects of preexisting flaws on the strength, deformation, and fracture behavior of rock specimens have been extensively investigated. Numerical methods offer a more flexible alternative for modeling the dynamic response of brittle rocks compared with experimental methods. Several studies have modeled the failure process of rocks with different preexisting flaw geometries. These numerical techniques mainly include continuous methods, discrete methods, and coupled methods. Tang and Kou[14] applied two numerical models to simulate crack behavior in brittle material as well as the effects of confining pressure and grain scale on rock cracks using the rock failure process analysis code, RFPA2D. Wong and Li[15,16] performed simulations using AUTODYN as the modeling tool and fully revealed the mechanism of crack types and coalescence

patterns in rocks containing two preexisting flaws. Haeri et al.[17] proposed a modified boundary element method to study crack behavior in the bridge area of brittle materials. Zhou et al.[18] used a phase-field method to determine the effect of preexisting flaws and interlayers on rock crack behavior. Huang et al.[19] used particle flow code (PFC) to reveal the effect of holes on the failure characteristic of granite, and typical crack coalescence patterns were obtained using their numerical method. Zhou et al.[20] used general particle dynamics to model the crack behavior of heterogeneous rocks containing multiple preexisting flaws. Their meshless numerical method displayed different crack types at or near the tips of these flaws. However, all of these methods are limited by various deficiencies with regard to capturing rock deformation and fracture processes. These deficiencies have been solved by the coupled method,[21,22] which combines the advantages of continuum and discontinuum techniques in a single code. The combined finite–discrete element method (FDEM) can simulate the interaction between discontinuous blocks and resolve the strain and stress fields within each discontinuous block. Gui et al.[23] used this coupled method to investigate the effect of flaw shape on rock crack behavior. Euser et al.[24] also used the combined FDEM to model fracture coalescence in flawed granite specimens. Han et al.[25] recently proposed the finite element method–cohesive zone model (FEM-CZM) method to reveal the shear deformation and crack behavior of rock-like materials containing fissure holes.

Holes and cracks are regarded as typical defects in natural rocks and affect the mechanical characteristics and crack behavior of rock materials under dynamic loading. The above studies significantly contributed to understanding the fracture mechanism for flawed rock materials. However, studies remain limited regarding the mechanical properties and crack behaviors of flawed rocks containing both holes and straight cracks under dynamic loading. The interaction between flaws in multi-flawed specimens is very complex and common in practice. Holes and cracks also have different influences on the rock mechanical properties, especially for rock dynamic problems. The mechanisms of hole–crack interactions and crack–crack interactions determine the progressive failure behavior of multi-flawed specimens under dynamic loading. These problems are not fully discussed in previous studies. The dynamic fracture behavior of multi-flawed specimens therefore requires further study to comprehensively understand the dynamic characteristics of natural multi-flawed rock.

In this paper, the flaw geometry in rock specimens is taken as a combination of perpendicular crack-like flaws, hole-like flaws, and inclined crack-like flaws. The continuum-based discrete element method (CDEM) is selected as the numerical tool to simulate dynamic crack behavior in flawed rock specimens. CDEM was proposed by Li et al.[26] and is a promising development in combined FEM/DEM methods. A dynamic fracture model incorporated into the traditional CDEM is also applied to reproduce tensile and inelastic shear cracks in rocks under dynamic loads. The accuracy of the presented numerical model is verified by a series of split Hopkinson pressure bar (SHPB) tests on flawed specimens. The effect of hole-like flaws on the dynamic fracture of multi-flawed granite is simulated.

2 | NUMERICAL METHOD AND EXPERIMENTAL SETUP

2.1 | Brief introduction of the traditional CDEM

The computational domain of CDEM is generally divided into different discrete blocks from an original intact block. As shown in Figure 1, these discontinuous blocks can be connected by virtual springs. The interaction between two blocks can be transformed into the spring force. When the virtual spring force reaches the given failure criterion, the continuous interface between the two blocks is transformed into a discontinuous fracture surface. In the traditional CDEM, the tensile crack behavior of blocks is governed by the maximum tensile stress criterion, and its shear strength is represented by the Mohr–Coulomb model.[27] Forces at the contact interface of two blocks in the local coordinate can be expressed as

$$F_n = -K_n \times \Delta u_n \tag{1}$$

$$F_s = -K_s \times \Delta u_s \tag{2}$$

where F, K, and Δu are the force, stiffness, and relative displacement of the virtual spring, respectively, and n and s represent the normal and tangential directions, respectively.

The spring was also used in the bond-based peridynamic, but their concepts are different. In the bond-based peridynamic, the Mode I fracture type and Mode II/III fracture type of springs are determined by the critical stretch of a spring and critical spring shear energy density, respectively.[28] However, in the CDEM, the tension spring and shear spring are established in the normal and tangential directions of the two block contact surfaces, respectively. In addition, the tension spring and shear spring are independent of each other in CDEM.

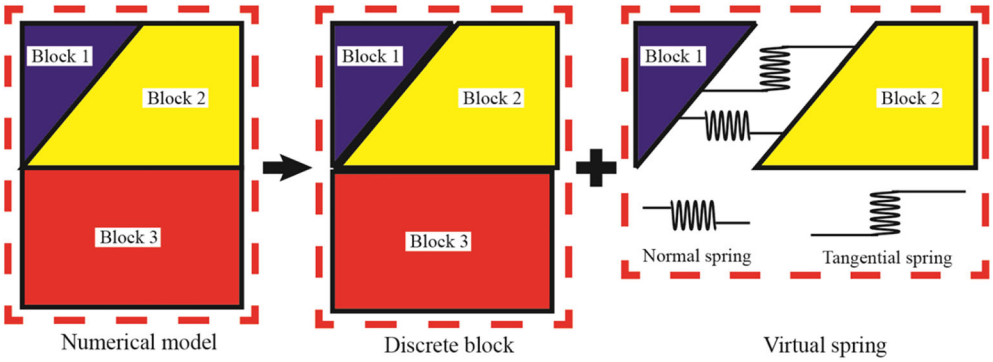

FIGURE 1 Discretization of the computational domain in the CDEM [Colour figure can be viewed at wileyonlinelibrary.com]

2.2 | Nonlinear dynamic fracture models

According to the shear strength model in the traditional CDEM,[26] the shear strength τ is given by the principal stresses as

$$\tau = \frac{\sigma_1 - \sigma_3}{2} \tag{3}$$

This model can also be given as a form of a pressure-sensitive model[29]:

$$\tau = \tau_0 + \alpha P \tag{4}$$

where τ_o is the shear strength of materials at pressure $P = 0$ and α represents sliding at the crack surfaces.

Rock materials under impact loading accumulate high localized stress in the impact location and exhibit high-pressure characteristics.[30] Tensile stress-induced failure plays a primary role near the low-stress zone. However, the shear strain of the material dominates the failure mechanism near the impacted zone.[31] When sufficient shear strain has accumulated, shear fracture begins to initiate in the rock. The fractured rock exerts high confinement pressure owing to the expanded volume of the broken rock.[32] To understand the dynamic shear response of brittle materials, Shafiq and Subhash[33] summarized and analyzed the strength characteristic of multiple brittle materials under dynamic loading conditions. Their study revealed the pressure-dependent shear deformation behavior of rock and limit of the linear pressure-sensitive model at high pressure. An extended Mohr–Coulomb model used to solve this limit was hence given as

$$\tau^* = a + be^{-kP^*} \tag{5}$$

where a, b, and k are model constants, which are 1.15, −1.06, and 1.78 for granite, respectively, $\tau^* = \tau/\tau_{HEL}$ and $P^* = P/P_{HEL}$ are the normalized shear strength and normalized hydrostatic pressure, respectively, and P_{HEL} and $\tau_{HEL} = \sigma_{HEL}/2$ are the pressure and equivalent shear stress at the Hugoniot elastic limit (HEL), respectively.

Pressure in brittle rock materials is usually decided by an equation of state (EOS), which defines the hydrostatic pressure–volume relationship under dynamic loads.[34] In this numerical model, a linear EOS is used for brittle rocks:

$$P = K\mu \tag{6}$$

where K is the bulk modulus, $\mu = (\rho/\rho_0) - 1$, and ρ and ρ_0 are the density of rock in the current state and initial states, respectively. It should also be noted that a virtual spring only represents the continuity status, but does not carry any mass. However, the pressure is continuous between the adjacent blocks prior to cracking. The pressure of a virtual spring is therefore taken as the average pressure of the two nodes it connects.

2.3 | Governing equations and contact algorithms

The mechanical equilibrium equation for element deformation in the CDEM, considering the effect of dynamic inertia, can be written in the following matrix form:

$$[M]\{u''\} + [C]\{u'\} + [K]\{u\} = \{F\}_{ext} \tag{7}$$

where $[M]$, $[C]$, and $[K]$ are the mass matrix, damping matrix, and stiffness matrix, respectively, and $\{F\}_{ext}$ is the external force vector in the integral domain of elements:

$$\{F\}_{ext} = \{F\}_b + \{F\}_s + \{F\}_t \tag{8}$$

where$\{F\}_b$, $\{F\}_S$, and $\{F\}_t$ denote the body force, spring force, and boundary traction in the integral domain of elements, respectively.

To efficiently calculate the nodal acceleration and nodal velocity of elements, CDEM uses an explicit scheme method in the integral domain[35]:

$$\{a\}^h = \frac{\{u\}^{h+1} - 2\{u\}^h + \{u\}^{h-1}}{(\Delta t)^2} \tag{9}$$

$$\{v\}^{h+1} = \frac{\{u\}^{h+1} - \{u\}^h}{\Delta t} \tag{10}$$

where h denotes the time step in the time integration of the CDEM and Δt represents the corresponding time step interval.

A combined semi-spring and semi-edge contact model by Feng et al.[36] is used in the CDEM to efficiently establish the virtual spring system. In this contact model, the location of semi-springs is near the vertices of each element. The distance between the semi-spring and corresponding vertices is usually 5% from the vertex to the center of each edge (two-dimensional) or surface (three-dimensional). When the virtual spring system is created, two adjacent virtual springs in each face are connected to form a semi-edge.[37] For a three-dimensional cube case, the cube has four semi-springs and four semi-edges in each surface of an element (Figure 2). The term "semi" here refers to a complete contact pair that cannot be created before a semi-spring or semi-edge locates its corresponding target surface or edge (Figure 3).

2.4 | Experimental verification of the improved CDEM

Rock is a complex natural material that contains various flaws, such as crack-like flaws and hole-like flaws. New cracks always initiate at these flaws and then coalesce with each other to ultimately form macroscale fractures. Rock crack behavior largely depends on the arrangement of preexisting flaws.[4] Flaw geometry is therefore very important for rock dynamic fracturing. To verify the accuracy of the presented model for simulating dynamic fracturing in rocks with random defects, rock specimens were prepared with a perpendicular crack-like flaw, an elliptical hole flaw, and an inclined crack-like flaw at different angles with respect to the loading direction. A granite specimen with a 75 mm diameter and 25 mm thickness was tested by the SHPB. The inclination angle between the center crack line and loading direction is 30°, 45°, and 60°, and other geometrical parameters are shown in Figure 4. The preexisting flaw is cut using a high-pressure water jet cutting device and kept approximately 1.0 mm wide in the specimens. The specimens were collected from the Fangshan area in Beijing, China. The rock properties of the Fangshan granite are given in Table 1.

An SHPB testing system was used to produce dynamic load conditions (Figure 5). The incident and transmitter bars in this work are both 2000 mm in length and 75 mm in diameter. Young's modulus, Poisson's ratio, and density of the bars are 210 GPa, 0.3, and 7800 kg/m^3, respectively. A strain gauge is glued on the bars to record the strain pulse induced in the laboratory tests. Based on one-dimensional stress wave theory and the stress equilibrium assumption, the analytical equations of the specimen strain, strain rate, and stress can be given as[38]

$$\sigma_s = \frac{A_b}{2A_s} E_b(\varepsilon_i + \varepsilon_r + \varepsilon_t) \tag{11}$$

$$\varepsilon_s = \frac{C_b}{L_s} \int_0^T (\varepsilon_i - \varepsilon_r - \varepsilon_t) dt \tag{12}$$

$$\varepsilon_s' = \frac{C_b}{L_s} (\varepsilon_i - \varepsilon_r - \varepsilon_t) \tag{13}$$

where A_b and A_S are the cross-sectional areas of the bar and specimen, respectively, C_b is the elastic wave speed in the bar, L_S is the specimen length, ε is the strain pulse, and the subscripts i, r, and t denote the incident, reflected, and transmitted pulses, respectively.

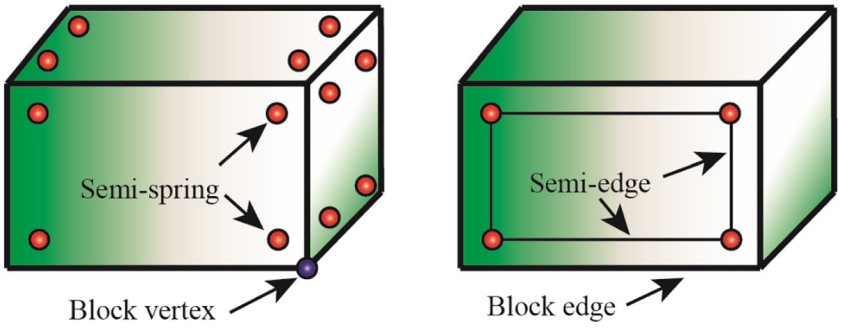

FIGURE 2 Illustration of semi-springs and semi-edges in a three-dimensional element of CDEM [Colour figure can be viewed at wileyonlinelibrary.com]

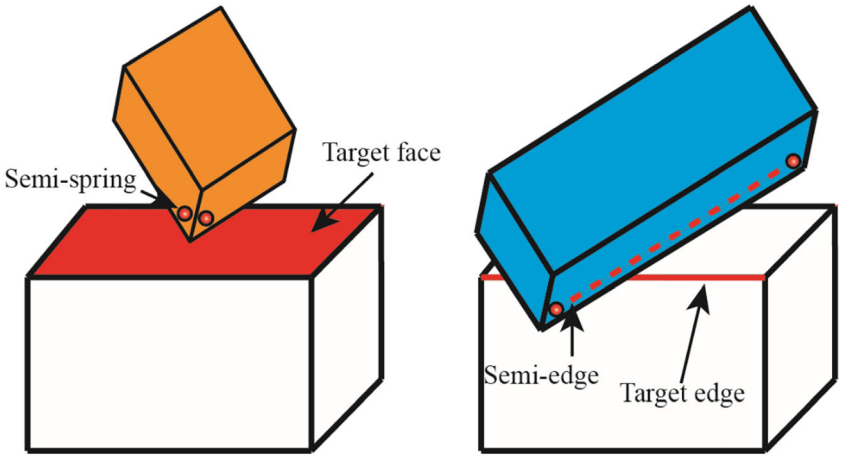

FIGURE 3 Contact model between blocks of CDEM [Colour figure can be viewed at wileyonlinelibrary.com]

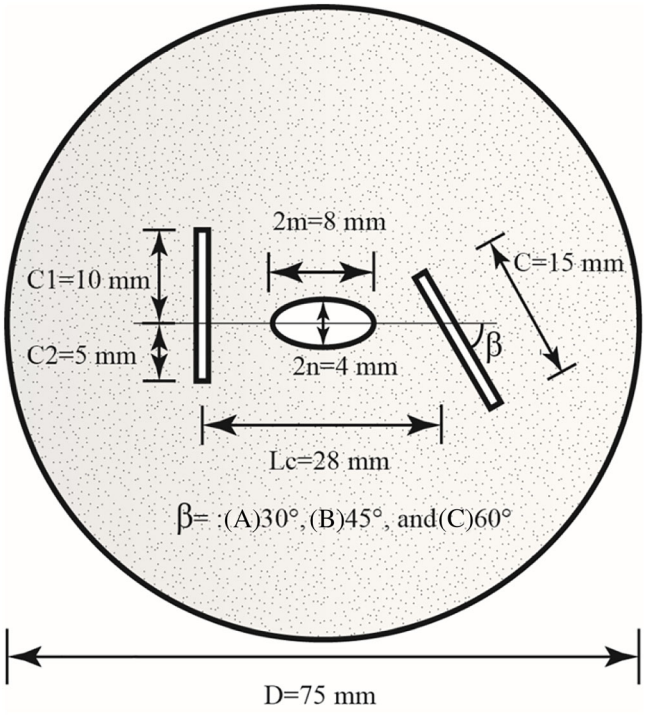

FIGURE 4 The geometry of specimens: (A) Specimen I, (B) Specimen II, and (C) Specimen III [Colour figure can be viewed at wileyonlinelibrary.com]

In the SHPB numerical model, an incident stress wave that evolves over time (Figure 6) is directly applied on the incident bar. To accurately simulate the intrinsic crack pattern, a maximum element size of 1 mm is used in the numerical model because rock fractures normally occur owing to fractures of mineral structures whose sizes are on the order of 10^{-4} to 10^{-3} m.[39] A combination of high-speed photography and the digital image correlation (DIC) method[40] was used in the SHPB test. Laboratory experiments on rock dynamics have shown that the DIC method can obtain qualitative and quantitative deformation characteristic of rock materials.[41–43]

A Kirana-5M high-speed camera was used in the tests, which can achieve a recording speed of 5×10^6 fps and thus a minimum interval between two successive photos of 200 ns. A μCMOS sensor is used in the Kirana camera to achieve high-speed acquisition without degrading the image resolution. The fixed image resolution is 924×768 pixels, and the acquisition number is 180. In our experimental tests, a recording speed of 5×10^5 fps was used, and the ratio of pixel to length is 0.1 mm/pixel. The region of interest is the entire image of the specimen for a better comparison with numerical simulation results. In addition, the high-intensity flash lamps were used to provide sufficient illumination for the surface of specimen. It is should be noted that an open-source DIC software (Ncorr) based on Matlab was used in our study to calculate full-field displacement. A comparison of the simulations and experiments with regard to the deformation and crack behavior observations of the multi-flawed granite specimens is shown in Table 2. The displacement fields and fracture patterns measured by the numerical method are in generally good agreement with the experimental results. This implies that the rock dynamic fracture process calculated by the improved CDEM is reasonable.

3 | SIMULATION RESULTS AND DISCUSSION

3.1 | Effects of hole-like flaws on the dynamic fracture of flawed rocks with different flaw geometries

Based on the above model verification, the effect of hole-like flaws on the dynamic fracture characteristic of flawed rocks is further investigated. The loading stress in the numerical simulation is determined by the experiment measurement. As indicated in Figure 6, the

TABLE 1 Basic rock properties of Fangshan granite

Young's modulus (GPa)	Poisson's ratio	Static tensile strength (MPa)	Density (kg/m^3)
44.9	0.22	12.8	3310

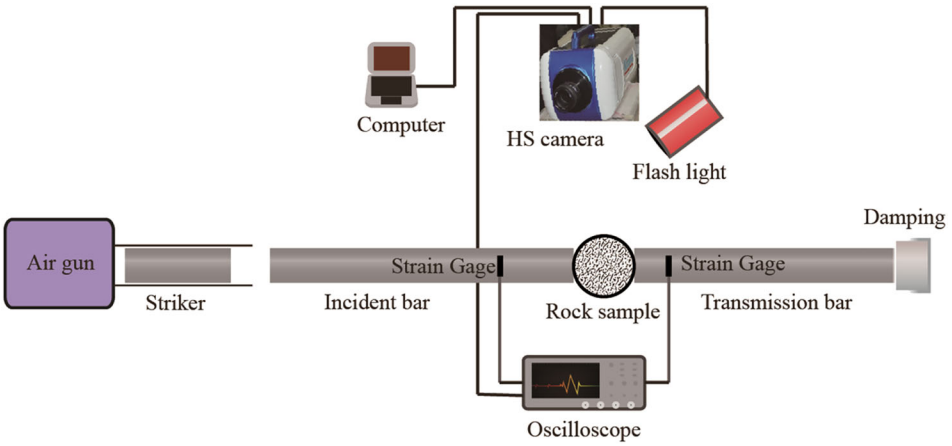

FIGURE 5 Schematic of the SHPB system combined with high-speed photography [Colour figure can be viewed at wileyonlinelibrary.com]

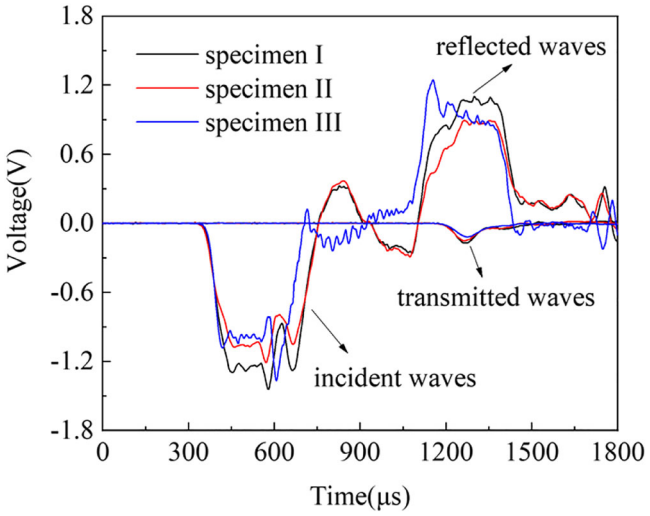

FIGURE 6 Waveform measured form SHPB tests for the three specimen [Colour figure can be viewed at wileyonlinelibrary.com]

measured incident waveform for the three specimens is not very consistent. To ensure that all of the numerical calculations are under the same loading conditions, the measured waveform of Model I is selected for loading the three specimens. To investigate the interaction between the hole-like flaw and two crack-like flaws, two paths were created along the two crack-like flaw. The maximum principal stress (σ_{max}) and maximum shear stress ($\sigma_{max} - \sigma_{min}$)/2 were calculated along this path. This stress-based approach has been verified to be an effective method for predicting crack initiation in flawed rocks.[44] Figure 7 shows the evolution of σ_{max} along the created path of the perpendicular crack-like flaw and inclined crack-like flaw. Very similar variations along the created path were observed at the perpendicular crack-like flaw in all of the specimens. The peak σ_{max} value is located at Point 5 in the crack region. However, the location of the peak σ_{max} value at the inclined crack-like flaw changes with increase of inclination angle. The shifting of the peak point could cause the deflection of crack initiation from the tip to the edge of the flaw. In the case of Specimen III, the calculated σ_{max} is much larger than that of other cases at the same time step. Figure 8 shows the evolution of the maximum shear stress along the created path of the two crack-like flaws. The numerical results indicate that the global peak value of the maximum shear stress along the created path is always located at the two flaw tips (Points 1 and 11). Interestingly, very similar variations of the maximum shear stress are observed along the created path of the perpendicular crack-like flaw in all of the specimens. This phenomenon is also noted in the evolution of σ_{max} at the perpendicular flaws. It can be therefore concluded that hole-like flaws can significantly weaken the interaction between two crack-like flaws. However, previous studies on flawed rock with this flaw geometry (i.e., two crack-like flaws) showed that variations of the inclined flaw angle have an apparent effect on the other flaw.[1,17,24] Although the fracture behavior of fractured rock with two preexisting cracks and a hole was investigated by Wu et al.,[45] the two preexisting cracks in their specimens changed synchronously. It was therefore difficult to detect a shielding effect of the hole-like flaw in their study and similar work.[46–48]

Shear cracks are rarely found in granite specimens, compared with tensile cracks, owing to the mineral

TABLE 2 Comparisons of simulations and experiments in three specimens

Legend	Simulation	DIC results	Crack patterns in camera
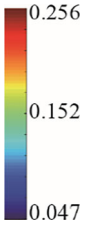	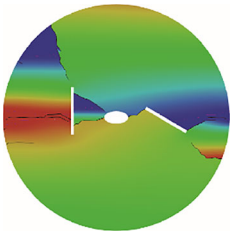	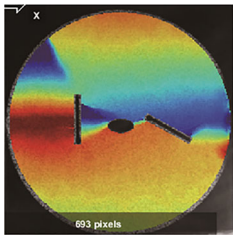	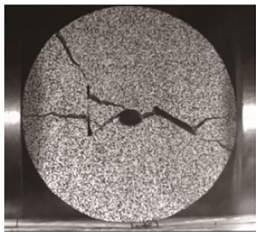
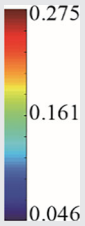	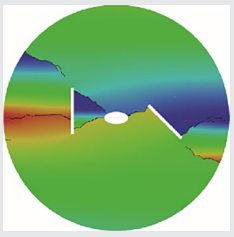	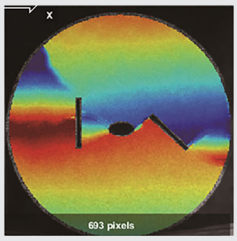	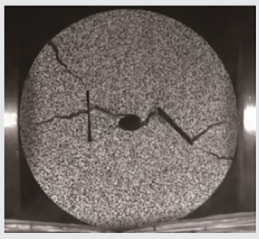
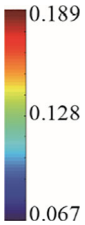	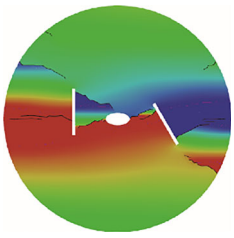	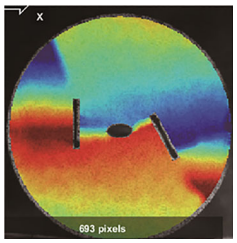	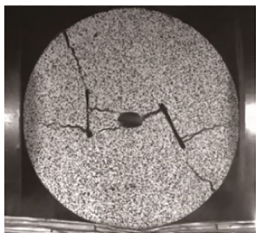

properties of granite.[49] Figures 7 and 8 show that the maximum shear force is less than σ_{max} in the crack region during the loading process. Tensile cracks therefore dominate the failure of granite specimens. Five cracks in four regions can be seen and summarized in Figure 9 based on the mechanical characteristics and crack propagation behavior of flawed rocks under impact loading.

Region I: The impact wave travels into the rock specimen through the loading end and further propagates toward the perpendicular crack-like flaw. When the wave front reaches this flaw, it begins to reflect back along the loading end direction. As the subjected stress reaches the rock tensile strength, the tensile crack (T_1) initiates at the edge of crack-like flaw. The cracking path near the preexisting flaw is not initially straight, and the crack propagation direction is initially nearly parallel to the loading direction.

Region II: When the incident wave impinges the perpendicular crack-like flaw, the flaw cannot completely block the incident wave. Near the two perpendicular flaw tips, there exists a diffracted wave on the side of the flaw surface. The stress wave then propagates between the crack-like flaw and hole-like flaw. Crack (T_2) ultimately initiates, deviating from the perpendicular flaw tip, and further grows approaching to the elliptical hole. Crack (T_3) subsequentially initiates at the elliptical hole and further reaches the perpendicular crack-like flaw.

Region III: Crack (T_4) in this region connects the hole-like flaw and inclined flaw. As the inclined flaw angle increases to 60°, the crack initiation at the inclined flaw shifts from the flaw tip to the edge, which has also been reported in other studies.[44,50,51]

Region IV: Crack (T_5) initiates at the inclined flaw. Upon further propagation, the curved growing crack front becomes gradually parallel to the transmission loading end. Crack initiation at the inclined flaw also shifts from the right tip to the edge as the inclined angle increases to 60°.

Three granite specimens were tested to verify experimental repeatability, with final crack patterns shown in Figure 9B. Due to anisotropy and inhomogeneity of rock specimens, it is difficult to obtain the completely same crack patterns among different specimens. However, in a qualitative view, final crack patterns of all specimens are similar, which are mainly distributed in the four regions mentioned above. Therefore, experimental results show good repeatability.

3.2 | Effects of holes on the dynamic fracture of flawed rocks under different loading conditions

Loading conditions have been shown to significantly affect the dynamic fracture of brittle rocks.[52–54] Different

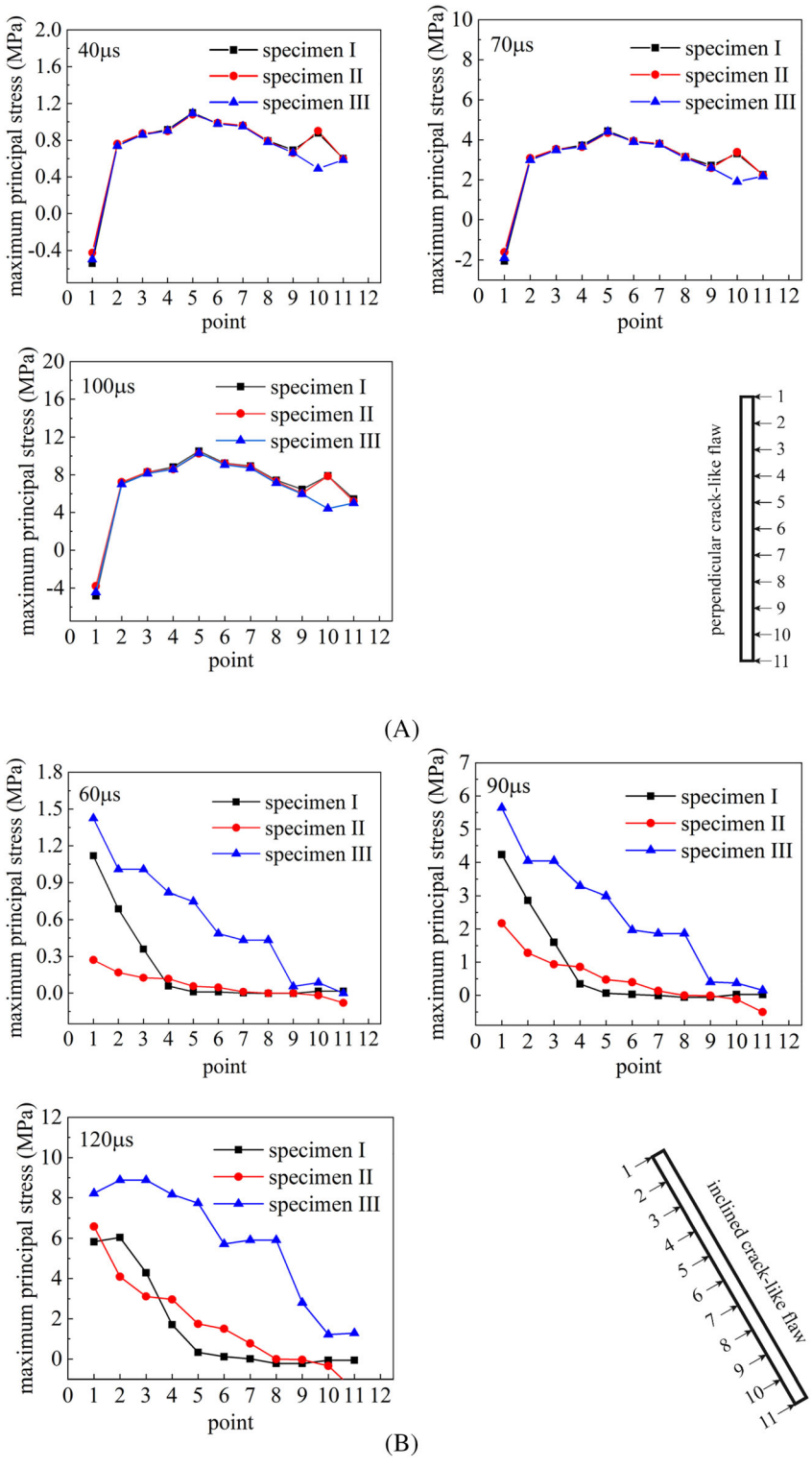

FIGURE 7 Evolution of the maximum principal stress along the two created paths [Colour figure can be viewed at wileyonlinelibrary.com]

loading conditions are therefore explored in the present numerical model to determine the effect of loading rate on the dynamic fracture of flawed rocks. Figure 10 shows the loading curves applied on the incident bar to load the flawed specimens. The maximum values of these stress waves are 50, 100, and 150 MPa, and all of the durations are 400 μs.

Figure 11 shows σ_{max} along the perpendicular path in all specimens. The duration of crack initiation decreases distinctly with increasing loading stress. However, a very similar variation of the calculated σ_{max} is observed along the created path in all specimens. Additionally, the variations of σ_{max} along the created path of a given specimen are very similar under different loading stresses.

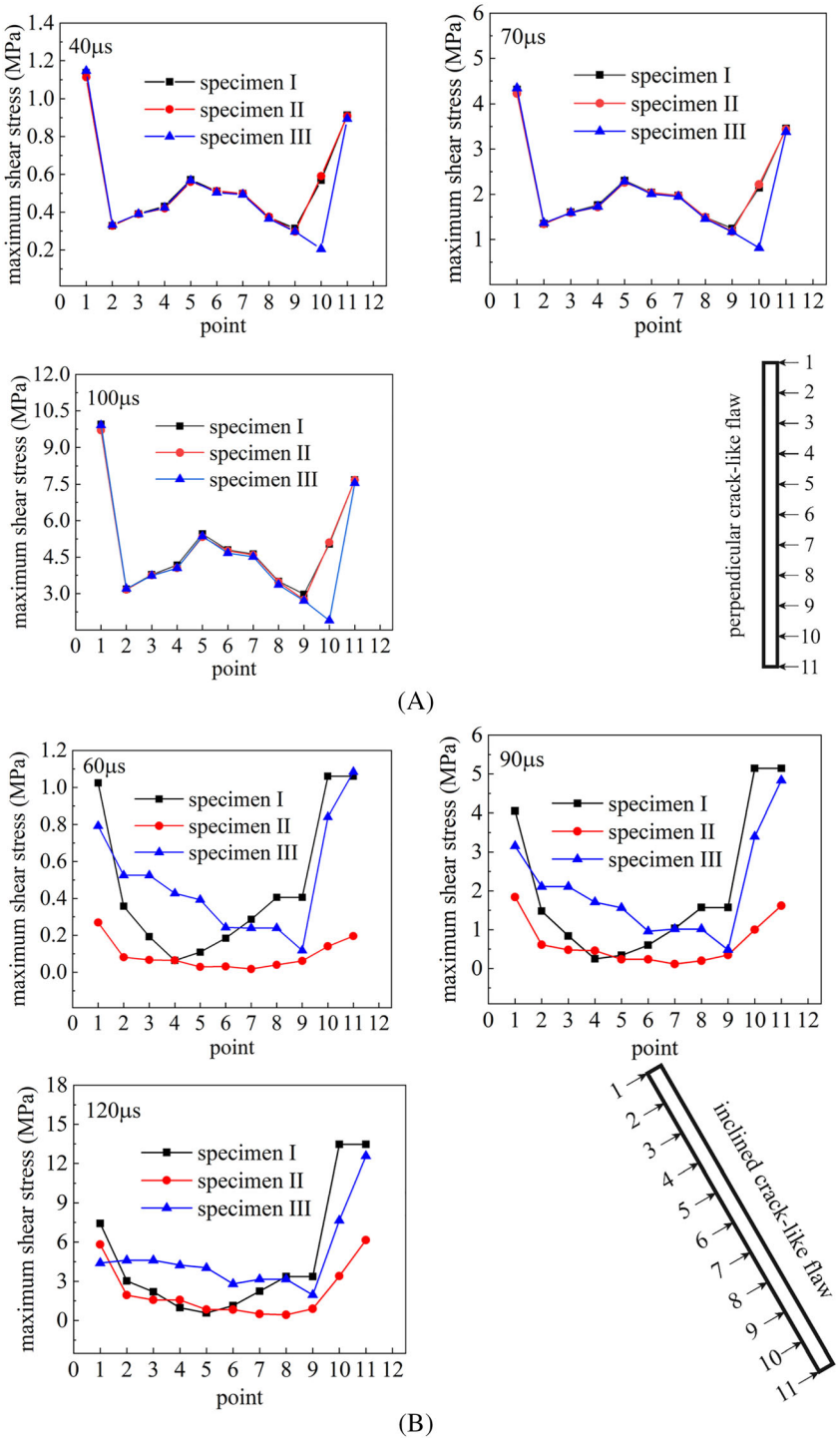

FIGURE 8 Evolution of the maximum shear stress along the two created paths [Colour figure can be viewed at wileyonlinelibrary.com]

Figure 12 shows the crack pattern of Specimen III under different loading stress conditions. The crack pattern morphology of the T_2 cracks shows notable changes in the different loading cases. The T_2 crack does not cease at the hole upon increasing loading stresses. The effect of the hole on crack coalescence of two crack-like flaws therefore gradually decreases with increasing loading stress.

4 | LIMITATIONS OF THE NUMERICAL MODEL AND FUTURE STUDIES

The CDEM approach presented herein is an improvement with respect to the traditional CDEM code, including the representation of nonlinear pressure-dependent shear strength of rocks under impact action. However,

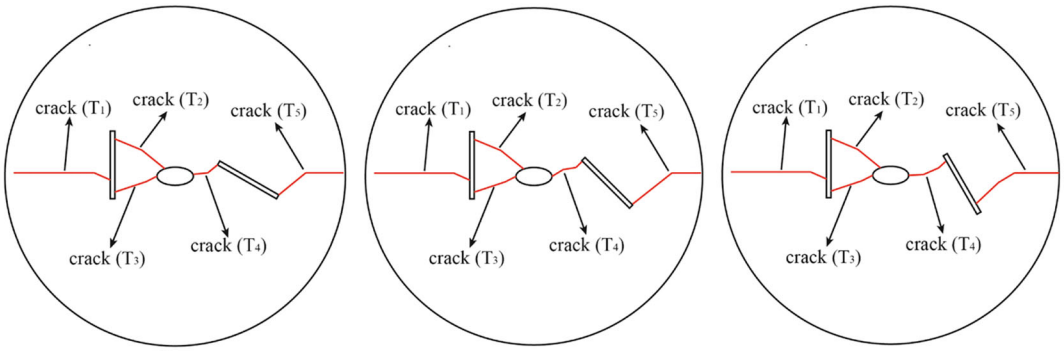

(A)

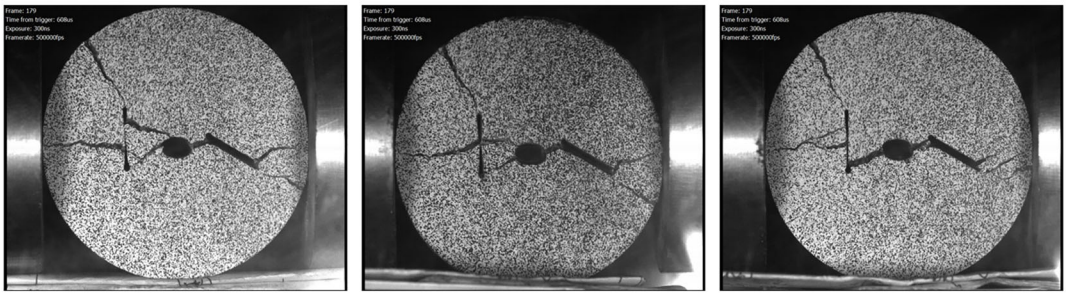

(B)

FIGURE 9 (A) Typical crack coalescence modes for all cases; (B) repeatability of experimental results [Colour figure can be viewed at wileyonlinelibrary.com]

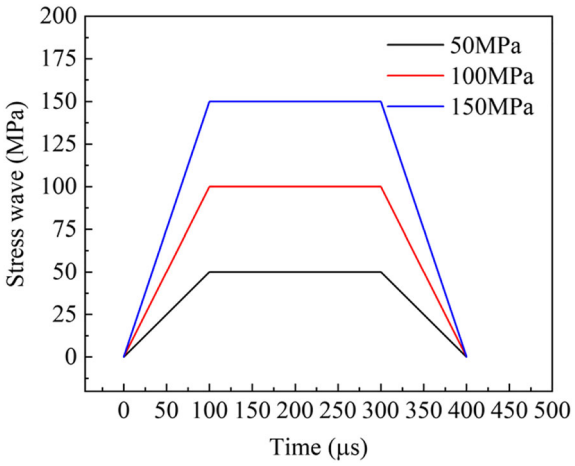

FIGURE 10 Loading curves in numerical simulations [Colour figure can be viewed at wileyonlinelibrary.com]

the numerical model is limited in the simulations of rock dynamic fracture behavior. In particular, crack formation in the numerical model is generated by the separation of two elements; hence, crack propagation is sensitive to the topology of the primary finite element mesh. Because adaptive re-meshing techniques are not implemented in this model, crack propagation is restricted along the predefined edge of the elements. The proposed numerical model also does not consider the rock specimen complexities (e.g., heterogeneities and natural defects aside from prefabrication defects). Further improvements are therefore underway to address these shortcomings.

5 | CONCLUSIONS

An improved CDEM model is proposed to consider the pressure-sensitive shear strength and tensile behavior of multi-flawed granite under impact loading. Verification tests are performed using the SHPB system. A granite model with different arrangements of preexisting flaws is simulated. The following conclusions can be drawn based on the simulation results.

1. Crack patterns in the flawed rock specimens predicted by the improved CDEM method are in good agreement with experimental observations obtained using high-speed photography. The measured DIC results indicate that the improved CDEM method can obtain qualitative and quantitative information regarding the

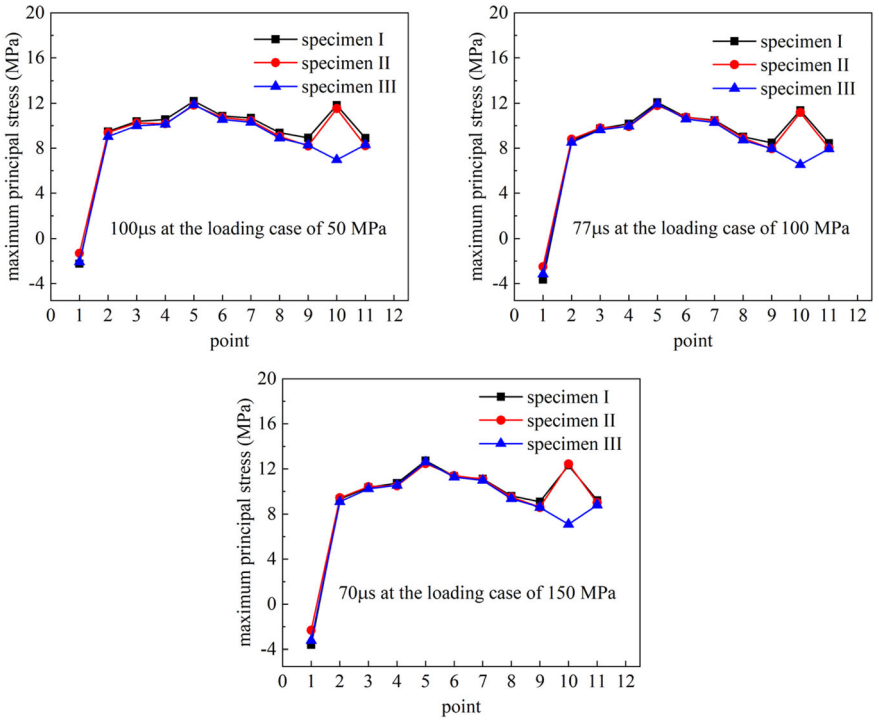

FIGURE 11 Maximum principal stress along the perpendicular path of flawed rocks [Colour figure can be viewed at wileyonlinelibrary.com]

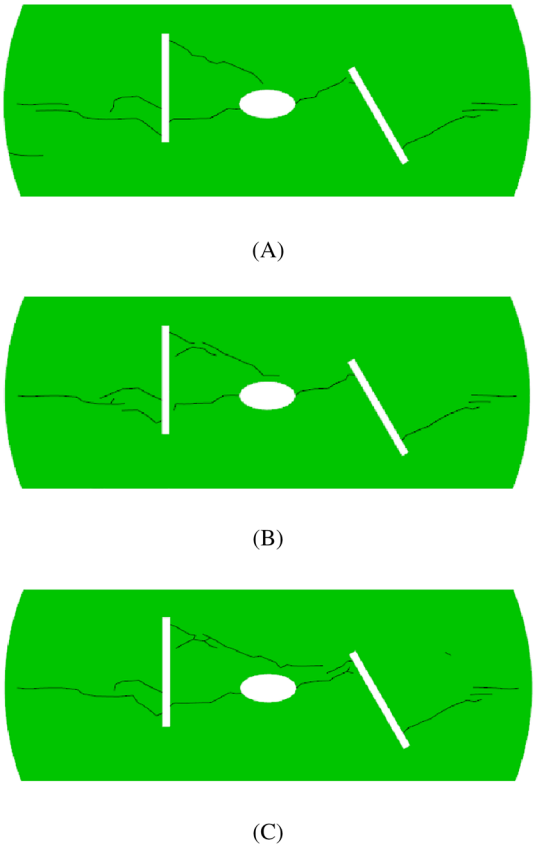

FIGURE 12 Crack patterns in Specimen III in the loading case of: (A) 50, (B) 100, and (C) 150 MPa [Colour figure can be viewed at wileyonlinelibrary.com]

deformation evolution of rock materials under impact loading.

2. Tensile cracks dominate the dynamic failure of the multi-flawed granite specimens in both the numerical simulations and experimental tests. Four crack patterns can be accordingly summarized: tensile cracks (T_1) between the incident loading end and perpendicular flaw; two tensile cracks (T_2 and T_3) between the perpendicular flaw and elliptical flaw; tensile cracks (T_4) between the elliptical flaw and inclined flaw; and tensile cracks (T_5) between the inclined flaw and transmission loading end.
3. The numerical calculated stresses and observed fracture patterns show that crack initiation at the inclined flaw shifts from the two tips to the edge with increasing inclination angle. However, the crack behavior between perpendicular crack-like flaws and hole-like flaws is slightly affected by variations of the flaw inclination angle.

Loading conditions significantly affect the dynamic characteristics of multi-flaw rocks. The effect of holes on the coalescence of two crack-like flaws gradually decreases with increasing loading stresses. These results provide important insights on the crack behavior and dynamic fracture mechanism of multi-flawed rocks, both of which are critical for geological engineering applications involving natural rock mass.

ACKNOWLEDGMENTS

The authors would like to acknowledge the anonymous reviewers for their constructive comments. This research was supported by the National Natural Science Foundation of China (No. 51974318).

CONFLICT OF INTEREST

The authors declare that they have no known competing financial interests or personal relationships that could have appeared to influence the work reported in this paper.

AUTHOR CONTRIBUTIONS

Zhongwen Yue: Funding acquisition, supervision, resources, writing-review and editing. Jun Zhou: Conceptualization, methodology, software, investigation, formal analysis, visualization, writing-original draft. Chun Feng: Software, writing-review and editing. Akang Li: Methodology, investigation, data curation. Peng Qiu: Supervision, writing-review and editing. Mingwei Gang: Investigation, data curation.

DATA AVAILABILITY STATEMENT

The data that support the findings of this study are openly available from authors upon request.

NOMENCLATURE

A_b	cross-sectional areas of bars
A_s	cross-sectional areas of specimens
a, b, k	constants in the extended Mohr–Coulomb model
{a}	acceleration
E_b	Young's modulus of bars
C	crack-like flaw length
C_b	elastic wave speed in bars
[C]	damping matrix
D	diameter of specimen disks
F_n	normal force
F_s	tangential force
{F}	external force vector
$\{F\}_b$	body force
$\{F\}_s$	spring force
$\{F\}_t$	boundary traction
HEL	Hugoniot elastic limit
K	bulk modulus
K_n	normal stiffness
K_s	normal stiffness
[K]	stiffness matrix
L_C	ligament length
L_s	specimen length
2m, 2n	elliptical hole axes
[M]	mass matrix
P	pressure
P^*	normalized hydrostatic pressure
P_{HEL}	pressure at HEL
{u}	displacement vector
{v}	velocity
α	sliding fraction constant
β	flaw inclination angle
Δt	time step interval
Δu_n	tangential displacement
Δu_s	tangential displacement
ε_i, ε_r, ε_t	incident, reflected, and transmitted strain pulses
ε_s	specimen strain
$\dot{\varepsilon}$	specimen strain rate
μ	volumetric strain
ρ	current rock density
ρ_0	initial rock density
σ_1, σ_2, σ_3	principal stresses
σ_{HEL}	equivalent stresses at HEL
σ_s	specimen stress
τ	shear strength
τ_0	shear strength at P = 0
τ_{HEL}	equivalent shear stress at HEL
τ^*	normalized shear strength

ORCID

Jun Zhou https://orcid.org/0000-0001-9180-3105
Peng Qiu https://orcid.org/0000-0003-0482-2899

REFERENCES

1. Lee H, Jeon S. An experimental and numerical study of fracture coalescence in pre-cracked specimens under uniaxial compression. *Int J Solid Struct*. 2011;48(6):979-999.
2. Li YP, Wang YH, Chen LZ. Experimental research on pre-cracked marble under compression. *Int J Solid Struct*. 2005;42(9):2505-2516.
3. Park CH, Bobet A. Crack coalescence in specimens with open and closed flaws: a comparison. *Int J Rock Mech Min Sci*. 2009;46(5):819-829.
4. Wong RHC, Chau KT, Tang CA, Lin P. Analysis of crack coalescence in rock-like materials containing three flaws—part I: experimental approach. *Int J Rock Mech Min Sci*. 2001;38(7):909-924.
5. Wong LNY, Einstein HH. Crack coalescence in molded gypsum and Carrara marble: part 1. macroscopic observations and interpretation. *Rock Mech Rock Eng*. 2009;42(3):475-511.
6. Park CH, Bobet A. Crack initiation, propagation and coalescence from frictional flaws in uniaxial compression. *Eng Fract Mech*. 2010;77(14):2727-2748.
7. Cao P, Liu T, Pu C, Lin H. Crack propagation and coalescence of brittle rock-like specimens with pre-existing cracks in compression. *Eng Geol*. 2015;187:113-121.
8. Brace WF, Bombolakis EG. A note on brittle crack growth in compression. *J Geophys Res*. 1963;68(12):3709-3713.

9. Bobet, Einstein HH. Fracture coalescence in rock-type materials under uniaxial and biaxial compression. *Int J Rock Mech Min Sci*. 1998;35(7):863-888.
10. Shen B, Stephansson O, Einstein HH, Ghahreman B. Coalescence of fractures under shear stresses in experiments. *J Geophys Res*. 1995;100(B4):5975-5990.
11. Wong RHC, Chau KT. Crack coalescence in a rock-like material containing two cracks. *Int J Rock Mech Min Sci*. 1998;35(2):147-164.
12. Huang YH, Yang SQ, Tian WL. Cracking process of a granite specimen that contains multiple pre-existing holes under uniaxial compression. *Fatigue Fract Eng Mater Struct*. 2019;42(6):1341-1356.
13. Huang YH, Yang SQ, Dong JP. Experimental study on fracture behaviour of three-flawed sandstone specimens after high-temperature treatments. *Fatigue Fract Eng Mater Struct*. 2020;43(10):2214-2231.
14. Tang CA, Kou SQ. Crack propagation and coalescence in brittle materials under compression. *Eng Fract Mech*. 1998;61(3):311-324.
15. Wong LNY, Li HQ. Numerical study on coalescence of two pre-existing coplanar flaws in rock. *Int J Solid Struct*. 2013;50(22):3685-3706.
16. Li HQ, Wong LNY. Numerical study on coalescence of pre-existing flaw pairs in rock-like material. *Rock Mech Rock Eng*. 2014;47(6):2087-2105.
17. Haeri H, Shahriar K, Marji MF, Moarefvand P. Experimental and numerical study of crack propagation and coalescence in pre-cracked rock-like disks. *Int J Rock Mech Min Sci*. 2014;67:20-28.
18. Zhou X, Jia Z, Berto F. Simulation of cracking behaviours in interlayered rocks with flaws subjected to tension using a phase-field method. *Fatigue Fract Eng Mater Struct*. 2019;42(8):1679-1698.
19. Huang Y, Yang S, Ranjith PG, Zhao J. Strength failure behavior and crack evolution mechanism of granite containing pre-existing non-coplanar holes: experimental study and particle flow modeling. *Comput Geotech*. 2017;88:182-198.
20. Zhou XP, Bi J, Qian QH. Numerical simulation of crack growth and coalescence in rock-like materials containing multiple pre-existing flaws. *Rock Mech Rock Eng*. 2015;48(3):1097-1114.
21. Munjiza A, Owen D, Bicanic N. A combined finite-discrete element method in transient dynamics of fracturing solids. *Eng Comput*. 1995;12(2):145-174.
22. Munjiza A, Bangash T, John NWM. The combined finite–discrete element method for structural failure and collapse. *Eng Fract Mech*. 2004;71(4-6):469-483.
23. Gui Y, Zhao Z, Zhang C, Ma S. Numerical investigation of the opening effect on the mechanical behaviours in rocks under uniaxial loading using hybrid continuum-discrete element method. *Comput Geotech*. 2017;90:55-72.
24. Euser B, Rougier E, Lei Z, et al. Simulation of fracture coalescence in granite via the combined finite–discrete element method. *Rock Mech Rock Eng*. 2019;52(9):3213-3227.
25. Han W, Jiang Y, Luan H, Du Y, Zhu Y, Liu J. Numerical investigation on the shear behavior of rock-like materials containing fissure-holes with FEM-CZM method. *Comput Geotech*. 2020;125:1-15, 103670.
26. Li S, Zhao M, Wang Y, Rao Y. A new numerical method for DEM–block and particle model. *Int J Rock Mech Min Sci*. 2004;41:414-418.
27. Feng C, Li S, Onate E. 2D particle contact-based meshfree method in CDEM and its application in geotechnical problems. *Eng Comput*. 2015;32(4):1080-1103.
28. Wang Y, Zhou X, Yuan W, Shou Y. A 3-D conjugated bond-pair-based peridynamic formulation for initiation and propagation of cracks in brittle solids. *Int J Solid Struct*. 2018;134:89-115.
29. Chen W, Ravichandran G. Failure mode transition in ceramics under dynamic multiaxial compression. *Int J Fract*. 2000;101(1–2):141-159.
30. Zhu Z, Mohanty B, Xie H. Numerical investigation of blasting-induced crack initiation and propagation in rocks. *Int J Rock Mech Min Sci*. 2007;44(3):412-424.
31. Ai H, Ahrens T. Simulation of dynamic response of granite: a numerical approach of shock-induced damage beneath impact craters. *Int J Impact Eng*. 2006;33(1–12):1-10.
32. Bavdekar S, Subhash G. Comparison of pressure-sensitive strength models for ceramics under ultrahigh confinement. *Int J Impact Eng*. 2018;118:60-66.
33. Shafiq M, Subhash G. An extended Mohr–Coulomb model for fracture strength of intact brittle materials under ultrahigh pressures. *J Am Ceram Soc*. 2016;99(2):627-630.
34. Zhou Q, Zhu Z, Wang X, Zhou J, Zhang X. The effect of a pre-existing crack on a running crack in brittle material under dynamic loads. *Fatigue Fract Eng Mater Struct*. 2019;42(11):2544-2557.
35. Wang L, Li S, Zhang G, Ma Z, Zhang L. A GPU-based parallel procedure for nonlinear analysis of complex structures using a coupled FEM/DEM approach. *Math Probl Eng*. 2013;12:841-860.
36. Feng C, Li S, Liu X, Zhang Y. A semi-spring and semi-edge combined contact model in CDEM and its application to analysis of Jiweishan landslide. *J Rock Mech Geotech Eng*. 2014;6(1):26-35.
37. Wang HZ, Bai CH, Feng C, Xue K, Zhu XG. An efficient CDEM-based method to calculate full-scale fragment field of warhead. *Int J Impact Eng*. 2019;133:1-16, 103331.
38. Meng H, Li QM. Correlation between the accuracy of a SHPB test and the stress uniformity based on numerical experiments. *Int J Impact Eng*. 2003;28(5):537-555.
39. Gui Y-L, Bui HH, Kodikara J, Zhang Q-B, Zhao J, Rabczuk T. Modelling the dynamic failure of brittle rocks using a hybrid continuum-discrete element method with a mixed-mode cohesive fracture model. *Int J Impact Eng*. 2016;87:146-155.
40. Chu TC, Ranson WF, Sutton MA. Applications of digital-image-correlation techniques to experimental mechanics. *Exp Mech*. 1985;25(3):232-244.
41. Zhang QB, Zhao J. A review of dynamic experimental techniques and mechanical behaviour of rock materials. *Rock Mech Rock Eng*. 2014;47(4):1411-1478.
42. Zhou XP, Lian YJ, Wong LNY, Berto F. Understanding the fracture behavior of brittle and ductile multi-flawed rocks by uniaxial loading by digital image correlation. *Eng Fract Mech*. 2018;199:438-460.
43. Zhou XP, Wang YT, Zhang JZ, Liu FN. Fracturing behavior study of three-flawed specimens by uniaxial compression and

3D digital image correlation: sensitivity to brittleness. *Rock Mech Rock Eng*. 2019;52(3):691-718.
44. Silva BGD, Einstein HH. Modeling of crack initiation, propagation and coalescence in rocks. *Int J Fracture*. 2013;182(2):167-186.
45. Wu T, Gao Y, Zhou Y, Li J. Experimental and numerical study on the interaction between holes and fissures in rock-like materials under uniaxial compression. *Theor Appl Fract Mech*. 2020;106:1-19, 102488.
46. Zhou XP, Zhang JZ, Wong L. Experimental study on the growth, coalescence and wrapping behaviors of 3d cross-embedded flaws under uniaxial compression. *Rock Mech Rock Eng*. 2018;51(5):1379-1400.
47. Zhou XP, Cheng H, Feng YF. An Experimental study of crack coalescence behaviour in rock-like materials containing multiple flaws under uniaxial compression. *Rock Mech Rock Eng*. 2014;47(6):1961-1986.
48. Zhang JZ, Zhou XP. AE event rate characteristics of flawed granite: from damage stress to ultimate failure. *Geophys J Int*. 2020;222(2):795-814.
49. Morgan SP, Johnson CA, Einstein HH. Cracking processes in Barre granite: fracture process zones and crack coalescence. *Int J Fract*. 2013;180(2):177-204.
50. Zou C, Wong LNY, Loo JJ, Gan BS. Different mechanical and cracking behaviors of single-flawed brittle gypsum specimens under dynamic and quasi-static loadings. *Eng Geol*. 2016;201:71-84.
51. Xie Y, Cao P, Liu J, Dong L. Influence of crack surface friction on crack initiation and propagation: a numerical investigation based on extended finite element method. *Comput Geotech*. 2016;74:1-14.
52. Lajtai EZ, Duncan EJS, Carter BJ. The effect of strain rate on rock strength. *Rock Mech Rock Eng*. 1991;24(2):99-109.
53. Zhang ZX, Kou SQ, Jiang LG, Lindqvist PA. Effects of loading rate on rock fracture: fracture characteristics and energy partitioning. *Int J Rock Mech Min Sci*. 2000;37(5):745-762.
54. Cho SH, Ogata Y, Kaneko K. Strain-rate dependency of the dynamic tensile strength of rock. *Int J Rock Mech Min Sci*. 2003;40(5):763-777.

How to cite this article: Yue Z, Zhou J, Feng C, Li A, Qiu P, Gang M. Numerical investigation of the effect of holes on dynamic fracturing in multi-flawed granite. *Fatigue Fract Eng Mater Struct*. 2021;1–14. https://doi.org/10.1111/ffe.13474